Low-Frequency Oscillation Analysis of VSM-Based VSC-HVDC Systems Based on the Five-Dimensional Impedance Stability Criterion

Guo, Jian; Chen, Yandong; Liao, Shuhan; Wu, Wenhua; Wang, Xiangyu; Guerrero, Josep M.

Published in:
IEEE Transactions on Industrial Electronics

DOI (link to publication from Publisher):
10.1109/TIE.2021.3076711

Publication date:
2022

Document Version
Accepted author manuscript, peer reviewed version

This article has been accepted for publication in a future issue of this journal, but has not been fully edited. Content may change prior to final publication. Citation information: DOI 10.1109/TIE.2021.3076711, IEEE Transactions on Industrial Electronics

Low-Frequency Oscillation Analysis of VSMs-Based VSC-HVDC Systems Based on the Five-Dimension Impedance Stability Criterion

Jian Guo, *Student Member*, *IEEE*, Yandong Chen, *Senior Member*, *IEEE*, Shuhan Liao, *Member*, *IEEE*, Wenhua Wu, *Member*, *IEEE*, Xiangyu Wang, *Student Member*, *IEEE*, and Josep M. Guerrero, *Fellow*, *IEEE*

***Abstract*—Virtual Synchronous Machines (VSMs)-based high voltage DC (HVDC) systems enhance the inertia of the power system. However, the dynamic interactions between the VSM-based rectifier station, the inverter station, and the grid could induce the system oscillation, which has been investigated in this paper. At first, the hybrid AC/DC impedance models of the VSMs considering the coupling between the AC and DC dynamics are established. Then, the relationships between the DC impedance, *dq*-frame impedance, and the hybrid AC/DC impedance are presented. It is found that the DC impedance of the VSM-based inverter station and the d-d channel impedance of the *dq*-frame impedance of the rectifier station behave as negative resistors in the low-frequency range. Moreover, a five-dimension impedance stability criterion based on the hybrid AC/DC impedance and generalized inverse Nyquist criterion is proposed to assess the system stability. The analysis results show that the low-frequency oscillation occurs when the grid SCR of the rectifier station is small. Finally, the simulation and experimental results verify the impedance models and the stability criterion.**

***Index Terms*—Impedance stability criterion; Virtual synchronous machine; VSC-HVDC system; Hybrid AC/DC impedance model**

NOMENCLATURE

L_f (L_{f1})	Filter inductor of the HVDC rectifier (inverter)
R_f (R_{f1})	Parasitic resistance of L_f (L_{f1})
U_{dc} (U_{dc1})	DC-link voltages of HVDC rectifier (inverter)
C_{dc}	DC-link capacitor of HVDC rectifier or inverter
L_{dc} (R_{dc})	DC-link line inductor (resistor)
u_{abc}	Three-phase voltages at PCC
u_α (u_β)	The $\alpha\beta$-frame voltage of u_{abc}
i_{abc1}	Input current of the HVDC rectifier
i_{abc}	Output current of the HVDC inverter
e_{abc}	Internal electric potential of VSM
ω_{ic} (ω_{vc})	Cutoff angular frequency of LPF of current sampling (voltage sampling)
f_0 (f_s)	Fundamental (switch) frequency
T_d	Control delay of VSM
J	Virtual inertia of VSM
D_q(D_p)	Reactive (Active) damping coefficient of VSM
K_i	Inertia gain of the reactive power loop of VSM
L_v (R_v)	Virtual inductor (resistor) of VSM
θ	Phase angle of the VSM
k_{pu} (k_{iu})	Proportional (integral) gain of voltage controllers of VSM
k_{pi1} (k_{ru})	Proportional (Resonance) gain of current controllers of VSM
ω_n	Rated angular frequency of the grid
ω_v	Angular frequency of the VSM
ω_r	Cutoff frequency of PR controller
δ	Phase difference between the VSM and the PCC
δ_0	Steady-state value of the δ
D_{d0} (D_{q0})	Steady-state values of duty ratio
U_{d0} (U_{q0})	Steady-state values of voltages
I_{d0} (I_{q0})	Steady-state values of currents
U_{dc0}	Steady-state value of dc-link voltage of the VSM
E_m	Output voltage magnitude of VSM
u_m	Voltage magnitude of the PCC
SCRi (SCRr)	Short circuit ratio at the inverter (rectifier) side

Manuscript received Nov 21, 2020; revised Feb 9, 2021; accepted Apr 17, 2021. This work was supported by the National Key Research and Development Program of China (2017YFB0902000), the National Natural Science Foundation of China (52077070), and the Science and Technology Innovation Program of Hunan Province (2020RC2033). *(Corresponding author: Yandong Chen.)*

Jian Guo, Yandong Chen, Shuhan Liao, Wenhua Wu, Leming Zhou, Zhiwei Xie, Xiangyu Wang, Zhikang Shuai are with the College of Electrical and Information Engineering, Hunan University, Changsha 410082, China (e-mail: yandong_chen@hnu.edu.cn.)

J. M. Guerrero is with the Department of Energy Technology, Aalborg University, Aalborg East 9220, Denmark.

I. INTRODUCTION

VOLTAGE source converter (VSC)-based high voltage DC (HVDC) systems have been generally utilized as transmission media to transfer power over a long distance [1]-

[2]. Due to the lack of inertia, the application of large quantities of the VSC-HVDC links changes the characteristics and threatens the stable operation of the power grid dominated by synchronous generators (SGs). Thus, the virtual synchronous machine (VSM)-based HVDC [3]-[6] system, which enables the rectifier station and the inverter station to simultaneously simulate the dynamic characteristics of synchronous generator, has been generally studied to provide the inertia and damping for the power system. It can be connected to the power grid friendly. However, the interactions between the VSM-based rectifier station, the inverter station, and the grid could cause the system oscillation, which needs to be further explored.

There are several tools widely used for the small-signal stability analysis of the HVDC system: the damping torque analysis method [6]-[7], the time-domain state-space method [8], and the impedance-based method [9]-[26]. The first and second methods need full knowledge of the hardware and control design of the converter, which are difficult to obtain due to commercial secrecy. By contrast, the impedance that can be measured is more suitable for stability analysis.

The impedance-based analysis methods can be divided into three categories: the DC impedance-based method [9]-[14], the AC impedance-based method [16]-[10], and the hybrid AC/DC impedance-based method [21]-[23]. Their common principle is to divide the system into two independent subsystems according to the source and load parts, and then apply the Nyquist stability criterion to the impedance ratio of the two subsystems. The DC impedance-based method is proposed in [9] for the first time to investigate the interactions of DC systems. Then, it is further utilized in the VSC-HVDC system [10]-[13]. Afterward, the detailed DC impedances of the VSC-HVDC system are developed with considering the control modes, and the phase-locked loop (PLL) [12], [14], etc. However, to the author's knowledge, the DC impedance modeling of the VSM-HVDC system has not been reported.

Originated from DC impedances, the AC impedance-based method has been extensively researched for power electronic converters-based systems. They are systematically classified based on the different frames, including the sequence impedance [15], the *dq*-frame impedance [16], the $\alpha\beta$–frame, etc. The *dq*-frame impedance [17] and the sequence impedance [18] are the most widely used for the VSC-HVDC system. They are essentially the same after considering the frequency coupling. For example, based on sequence impedances, studies in [18] show that the VSM without inner loops behaves inductive and can run stably in a weak grid. Based on *dq*-frame impedances, the subsynchronous oscillation of the VSM with the DC voltage loop and inner loops is studied in [19]. However, the DC dynamics effects exerting on AC impedances remain unknown when the VSC-HVDC system operates as VSMs.

The above stability analyses ignore the coupling between the AC and DC dynamics, and the stability analysis of the VSC-HVDC system by using the DC or AC impedance is difficult to deal with the right half-plane (RHP) poles. To solve these issues, the hybrid AC/DC impedance is first proposed in [21], and the promising stability criteria of the VSC-HVDC system based on the hybrid AC/DC impedance are proposed in [21]-[24]. A stability analysis method of the modular multilevel converter (MMC)-HVDC systems for the wind farm integration based on the three-by-three ratio matrix is proposed in [22], but the RHP poles of the DC impedance of grid-side MMC is still difficult to deal with. Thus, a six-dimension stability criterion is proposed in [23] to solve the issues of the RHP poles. However, the calculation of the six characteristic loci is quite complicated. Besides, the hybrid AC/DC impedance model in [23] contains no DC-link capacitor filters. If the DC-link capacitor filters are considered in the modeling, the stability criterion is unavailable because (47) in [23] has no inverse transformation.

To address the aforementioned issues, this paper investigates the stability of the VSM-based HVDC system by using the hybrid AC/DC impedances and the proposed five-dimension impedance stability criterion. The main contributions are:

1) The hybrid AC/DC impedance models of the VSM-based rectifier station and inverter station are established and verified.

2) The DC and *dq*-frame impedance models of VSMs are established based on the hybrid AC/DC impedance models, and their impedance characteristics are compared.

3) The five-dimension impedance stability criterion based on the hybrid AC/DC impedance models and the generalized inverse Nyquist criterion (GINC) is proposed to analyze the stability of the VSM-based HVDC systems, and the low-frequency oscillation of the system is revealed.

The rest of the paper is organized as follows: Section II presents the description of the HVDC system based on VSMs. Section III establishes the hybrid AC/DC impedance models of the VSMs. Section IV presents the transformation between the hybrid AC/DC impedance, *dq*-frame impedance, and DC impedance. Section V contains the proposed five-dimension impedance stability criterion, the stability analysis, and the experimental results. Section VI presents the brief conclusions.

II. System Description

Figure 1(a) illustrates the VSMs-based VSC-HVDC systems, where variables with an asterisk (*) correspond to reference signals. The system parameters of the rectifier station and inverter station are the same, as shown in Table I of section IV. Since this paper focuses on the control method effects exerting on the system stability, a two-level VSC-HVDC system is investigated. One key feature of VSMs is that the rotor swing equation is used for the synchronization and inertia emulation so that the converter can share similar dynamics to SGs [6]. The reactive power controller simulates primary voltage regulations of synchronous machines, and the active power controller emulates the inertia and primary frequency regulation of synchronous machines:

$$\omega_{\mathrm{n}}-\omega_{\mathrm{v}}=\frac{P^{*}-P}{(Js+D_{\mathrm{p}})\omega_{\mathrm{n}}} \tag{1}$$

$$E_{\mathrm{m}}=(D_{\mathrm{q}}(u_{\mathrm{d}}^{*}-u_{\mathrm{d}})+Q^{*}-Q)/(Ks) \tag{2}$$

The ac voltage controllers of the VSM adopt the virtual impedance to emulate the electrical part of synchronous machines [27], and L_{v} and R_{v} are the virtual resistor and inductor, respectively. Besides, the current controllers adopt PR regulators in the $\alpha\beta$ frame.

The only difference between the VSM rectifier and inverter is the dc-link voltage controller:

$$P^{*}=-(u_{\mathrm{dc}}^{*}-u_{\mathrm{dc}})u_{\mathrm{dc}}^{*}(k_{\mathrm{pu}}+k_{\mathrm{iu}}/s) \tag{3}$$

The output voltage magnitude (u_{m}), the active power (P), and

This article has been accepted for publication in a future issue of this journal, but has not been fully edited. Content may change prior to final publication. Citation information: DOI 10.1109/TIE.2021.3076711, IEEE Transactions on Industrial Electronics

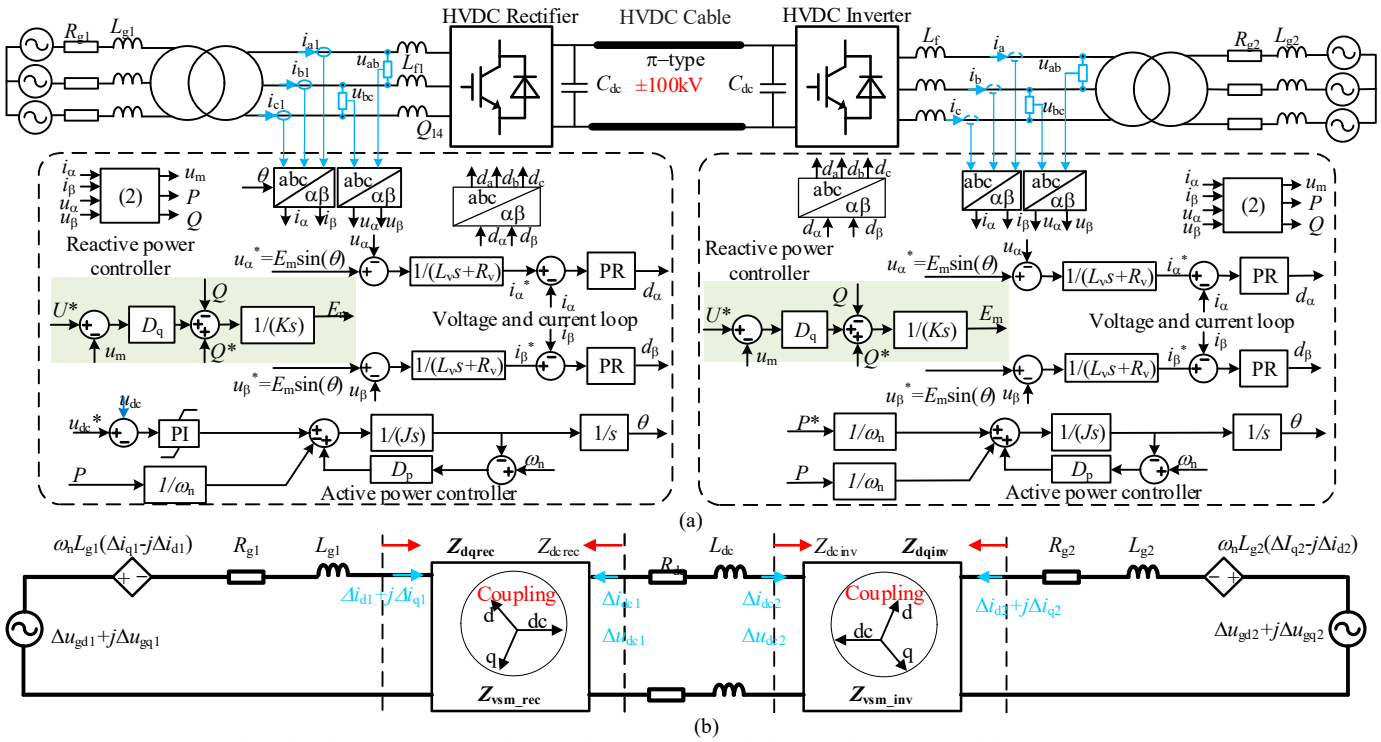

Fig. 1 VSC-HVDC systems based on the VSMs. (a) Typical circuit diagram and control; (b) Equivalent circuit model.

the reactive power (Q) of the VSM are expressed as follows:

$$\begin{cases} u_{\mathrm{m}} = \sqrt{u_\alpha{}^2 + u_\beta{}^2} \\ P = \dfrac{3}{2}(u_\alpha i_\alpha + u_\beta i_\beta) \\ Q = \dfrac{3}{2}(u_\alpha i_\beta - u_\beta i_\alpha) \end{cases} \tag{4}$$

Figure 1(b) illustrates the equivalent circuit model of the VSC-HVDC system, where DC impedances of the rectifier and inverter (Z_{dcrec}, Z_{dcinv}), dq-frame impedances of the rectifier and inverter ($\boldsymbol{Z}_{\mathbf{dqrec}}$, $\boldsymbol{Z}_{\mathbf{dqinv}}$), and the hybrid AC/DC impedances of the rectifier and inverter ($\boldsymbol{Z}_{\mathbf{vsm\_rec}}$, $\boldsymbol{Z}_{\mathbf{vsm\_inv}}$) will be used later.

III. Hybrid AC/DC Impedance Modeling of the VSMs

A. Small-Signal Model of Main Circuit

The main circuit of the converter as shown in Fig. 1(a) can be modeled as follows:

$$\begin{cases} L_{\mathrm{f}}\dfrac{di_{\mathrm{d}}}{dt} - \omega_{\mathrm{n}} L_{\mathrm{f}} i_{\mathrm{q}} + i_{\mathrm{d}} R_{\mathrm{f}} = d_{\mathrm{d}} u_{\mathrm{dc}}/2 - u_{\mathrm{d}} \\ L_{\mathrm{f}}\dfrac{di_{\mathrm{q}}}{dt} + \omega_{\mathrm{n}} L_{\mathrm{f}} i_{\mathrm{d}} + i_{\mathrm{q}} R_{\mathrm{f}} = d_{\mathrm{q}} u_{\mathrm{dc}}/2 - u_{\mathrm{q}} \\ C_{\mathrm{dc}}\dfrac{du_{\mathrm{dc}}}{dt} = -\dfrac{3}{4}(d_{\mathrm{d}} i_{\mathrm{d}} + d_{\mathrm{q}} i_{\mathrm{q}}) - i_{\mathrm{dc}} \end{cases} \tag{5}$$

The small-signal model of (5) can be expressed as follows:

$$\begin{bmatrix} D_{\mathrm{d0}} \\ D_{\mathrm{q0}} \end{bmatrix} \frac{\Delta u_{\mathrm{dc}}}{2} + \frac{U_{\mathrm{dc0}}}{2}\begin{bmatrix} \Delta d_{\mathrm{d}} \\ \Delta d_{\mathrm{q}} \end{bmatrix} - \begin{bmatrix} \Delta u_{\mathrm{d}} \\ \Delta u_{\mathrm{q}} \end{bmatrix} = \boldsymbol{Z}_{\mathbf{1}} \begin{bmatrix} \Delta i_{\mathrm{d}} \\ \Delta i_{\mathrm{q}} \end{bmatrix} \tag{6}$$

$$\Delta u_{\mathrm{dc}} = -\frac{3}{4C_{\mathrm{dc}}s}\left([D_{\mathrm{d0}}\ D_{\mathrm{q0}}] \begin{bmatrix} \Delta i_{\mathrm{d}} \\ \Delta i_{\mathrm{q}} \end{bmatrix} - [I_{\mathrm{d0}}\ I_{\mathrm{q0}}] \begin{bmatrix} \Delta d_{\mathrm{d}} \\ \Delta d_{\mathrm{q}} \end{bmatrix} \right) - \frac{\Delta i_{\mathrm{dc}}}{C_{\mathrm{dc}}s} \tag{7}$$

where "Δ" denotes the small-signal perturbation of a variable.

The small-signal model of the main circuit by embedding (7) into (6) can be re-written as follows:

$$\begin{bmatrix} \Delta u_{\mathrm{d}} \\ \Delta u_{\mathrm{q}} \end{bmatrix} = -\boldsymbol{G}_{\mathbf{1}} \begin{bmatrix} \Delta i_{\mathrm{d}} \\ \Delta i_{\mathrm{q}} \end{bmatrix} + \boldsymbol{G}_{\mathbf{2}} \begin{bmatrix} \Delta d_{\mathrm{d}} \\ \Delta d_{\mathrm{q}} \end{bmatrix} - \boldsymbol{G}_{\mathbf{3}} \Delta i_{\mathrm{dc}} \tag{8}$$

where $\boldsymbol{G}_{\mathbf{1}}$, $\boldsymbol{G}_{\mathbf{2}}$, and $\boldsymbol{G}_{\mathbf{3}}$ can be represented as follows:

$$\begin{cases} \boldsymbol{G}_{\mathbf{1}} = \boldsymbol{Z}_{\mathbf{1}} + \dfrac{3}{8C_{\mathrm{dc}}s}\begin{bmatrix} D_{\mathrm{d0}}^2 & D_{\mathrm{d0}}D_{\mathrm{q0}} \\ D_{\mathrm{d0}}D_{\mathrm{q0}} & D_{\mathrm{q0}}^2 \end{bmatrix} \\ \boldsymbol{G}_{\mathbf{2}} = \dfrac{1}{2}\begin{bmatrix} U_{\mathrm{dc0}} & 0 \\ 0 & U_{\mathrm{dc0}} \end{bmatrix} - \dfrac{3}{8C_{\mathrm{dc}}s}\begin{bmatrix} D_{\mathrm{d0}}I_{\mathrm{d0}} & D_{\mathrm{d0}}I_{\mathrm{q0}} \\ D_{\mathrm{q0}}I_{\mathrm{d0}} & D_{\mathrm{q}}I_{\mathrm{q0}} \end{bmatrix} \\ \boldsymbol{G}_{\mathbf{3}} = \dfrac{1}{2C_{\mathrm{dc}}s}\begin{bmatrix} D_{\mathrm{d0}} \\ D_{\mathrm{q0}} \end{bmatrix} \end{cases} \tag{9}$$

Finally, the small-signal model of the main circuit according to (7) and (8) is expressed as follows:

$$\begin{bmatrix} \Delta i_{\mathrm{d}} \\ \Delta i_{\mathrm{q}} \\ \Delta i_{\mathrm{dc}} \end{bmatrix} = \boldsymbol{F}_{\mathbf{1}}^{-1} \left(\boldsymbol{F}_{\mathbf{2}} \begin{bmatrix} \Delta d_{\mathrm{d}} \\ \Delta d_{\mathrm{q}} \\ 0 \end{bmatrix} - \begin{bmatrix} \Delta u_{\mathrm{d}} \\ \Delta u_{\mathrm{q}} \\ \Delta u_{\mathrm{dc}} \end{bmatrix} \right) \tag{10}$$

where $\boldsymbol{F}_{\mathbf{1}}$ and $\boldsymbol{F}_{\mathbf{2}}$ are represented as follows:

$$\boldsymbol{F}_{\mathbf{1}} = \begin{bmatrix} \multicolumn{2}{c}{\boldsymbol{G}_{\mathbf{1}}} & \boldsymbol{G}_{\mathbf{3}} \\ \dfrac{3D_{\mathrm{d0}}}{4C_{\mathrm{dc}}s} & \dfrac{3D_{\mathrm{q0}}}{4C_{\mathrm{dc}}s} & \dfrac{1}{C_{\mathrm{dc}}s} \end{bmatrix} \tag{11}$$

$$\boldsymbol{F}_{\mathbf{2}} = \begin{bmatrix} \multicolumn{2}{c}{\boldsymbol{G}_{\mathbf{2}}} & \boldsymbol{0} \\ -\dfrac{3I_{\mathrm{d0}}}{4C_{\mathrm{dc}}s} & -\dfrac{3I_{\mathrm{q0}}}{4C_{\mathrm{dc}}s} & 0 \end{bmatrix} \tag{12}$$

B. Hybrid AC/DC Impedance Modeling of the VSM

The controllers, the control delay, and voltage and current sampling filters, which are all in static coordinates, need to be

This article has been accepted for publication in a future issue of this journal, but has not been fully edited. Content may change prior to final publication. Citation information: DOI 10.1109/TIE.2021.3076711, IEEE Transactions on Industrial Electronics

transformed to the synchronous frame. Assuming that the transfer function in static coordinates is $H_1(s)$, the expression converted to a *dq* frame is given as follows [29]:

$$\begin{cases} \boldsymbol{H}_{\mathbf{dq}} = \dfrac{1}{2}\begin{bmatrix} A+B & -j(A-B) \\ j(A-B) & A+B \end{bmatrix} \\ A = H_1(s+j\omega_{\mathrm{n}}) \quad B = H_1(s-j\omega_{\mathrm{n}}) \end{cases} \tag{13}$$

The three by three matrix of the control delay based on (13) and the Euler formula is obtained as follows:

$$\boldsymbol{G}_{\mathbf{del}} = e^{-T_{\mathrm{d}}s}\begin{bmatrix} \cos(\omega_{\mathrm{n}}T_{\mathrm{d}}) & \sin(\omega_{\mathrm{n}}T_{\mathrm{d}}) & 0 \\ -\sin(\omega_{\mathrm{n}}T_{\mathrm{d}}) & \cos(\omega_{\mathrm{n}}T_{\mathrm{d}}) & 0 \\ 0 & 0 & 0 \end{bmatrix} \tag{14}$$

Similarly, the first-order low-pass filters for voltage or current signals are expressed as follows:

$$\boldsymbol{K}_{\mathbf{x}} = \begin{bmatrix} \dfrac{1+T_{\mathrm{x}}s}{(1+T_{\mathrm{x}}s)^2+(\omega_{\mathrm{n}}T_{\mathrm{x}})^2} & \dfrac{\omega_{\mathrm{n}}T_{\mathrm{x}}}{(1+T_{\mathrm{x}}s)^2+(\omega_{\mathrm{n}}T_{\mathrm{x}})^2} & 0 \\ \dfrac{-\omega_{\mathrm{n}}T_{\mathrm{x}}}{(1+T_{\mathrm{x}}s)^2+(\omega_{\mathrm{n}}T_{\mathrm{x}})^2} & \dfrac{1+T_{\mathrm{x}}s}{(1+T_{\mathrm{x}}s)^2+(\omega_{\mathrm{n}}T_{\mathrm{x}})^2} & 0 \\ 0 & 0 & \dfrac{1}{1+T_{\mathrm{x}}s} \end{bmatrix} \tag{15}$$

Besides, the current controller can be expressed as follows:

$$\begin{cases} \boldsymbol{G}_{\mathbf{ic}} = \dfrac{1}{C}\begin{bmatrix} C_1 & C_2 & 0 \\ C_2 & C_1 & 0 \\ 0 & 0 & 0 \end{bmatrix} \\ C_1 = k_{\mathrm{p}} + 2k_{\mathrm{r}}\omega_{\mathrm{r}}(2s^3 + 4\omega_{\mathrm{n}}s^2 + 4\omega_{\mathrm{n}}{}^2 s + 4\omega_{\mathrm{r}}\omega_{\mathrm{n}}{}^2) \\ C_2 = 2k_{\mathrm{r}}\omega_{\mathrm{r}}(2s^3 + 4\omega_{\mathrm{n}}s^2 + 4\omega_{\mathrm{n}}{}^2 s + 4\omega_{\mathrm{r}}\omega_{\mathrm{n}}{}^2) \\ C = s^4 + 4\omega_{\mathrm{r}}s^3 + 4(\omega_{\mathrm{r}}{}^2 + \omega_{\mathrm{n}}{}^2)s^2 + 8\omega_{\mathrm{r}}\omega_{\mathrm{n}}{}^2 s + 4\omega_{\mathrm{r}}{}^2\omega_{\mathrm{n}}{}^2 \end{cases} \tag{16}$$

In addition, the equivalent three-by-three matrix of the voltage controller is derived as follows:

$$\boldsymbol{G}_{\mathbf{uc}} = \begin{bmatrix} \boldsymbol{Z}_{\mathbf{lv}}{}^{-1} & & 0 \\ & & 0 \\ 0 & 0 & 0 \end{bmatrix} \tag{17}$$

where $\boldsymbol{Z}_{\mathbf{lv}}$ is the dq impedance of the virtual inductor.

As shown in Fig. 2, $\boldsymbol{G}_{\mathbf{dc}}$ representing the dc-link voltage controller is denoted by a three-by-three transfer matrix:

$$\boldsymbol{G}_{\mathbf{dc}} = \begin{bmatrix} 0 & 0 & -\omega_{\mathrm{n}}\left(k_{\mathrm{pu}}+k_{\mathrm{iu}}\right)/s \\ 0 & 0 & 0 \\ 0 & 0 & 0 \end{bmatrix} \tag{18}$$

Add the *dq*-frame small-signal disturbances to active and reactive power controllers:

$$\begin{bmatrix} \Delta\theta \\ \Delta E_{\mathrm{m}} \end{bmatrix} = -\begin{bmatrix} \dfrac{1}{(Js^2+D_{\mathrm{p}}s)\omega_{\mathrm{n}}} & 0 \\ 0 & \dfrac{1}{Ks} \end{bmatrix}\begin{bmatrix} \Delta P \\ \Delta Q \end{bmatrix} - \begin{bmatrix} 0 & 0 \\ \dfrac{D_{\mathrm{q}}}{Ks} & 0 \end{bmatrix}\begin{bmatrix} \Delta u_{\mathrm{d}} \\ \Delta u_{\mathrm{q}} \end{bmatrix} \tag{19}$$

Then, $\boldsymbol{F}_{\mathbf{PQ}}$ and $\boldsymbol{M}$ are defined as follows:

$$\boldsymbol{F}_{\mathbf{PQ}} = \begin{bmatrix} 1/(J\omega_{\mathrm{n}}s^2 + D_{\mathrm{p}}\omega_{\mathrm{n}}s) & 0 & 0 \\ 0 & 1/(Ks) & 0 \\ 0 & 0 & 0 \end{bmatrix} \tag{20}$$

$$\boldsymbol{M} = \begin{bmatrix} 0 & 0 & 0 \\ D_{\mathrm{q}}/(Ks) & 0 & 0 \\ 0 & 0 & 0 \end{bmatrix} \tag{21}$$

Adding the *dq*-frame small-signal disturbances to the instantaneous active and reactive power calculation, $\boldsymbol{F}_{\mathbf{i}}$ and $\boldsymbol{F}_{\mathbf{u}}$ are defined as follows:

$$\boldsymbol{F}_{\mathbf{i}} = \frac{3}{2}\begin{bmatrix} U_{\mathrm{d0}} & U_{\mathrm{q0}} & 0 \\ U_{\mathrm{q0}} & U_{\mathrm{q0}} & 0 \\ 0 & 0 & 0 \end{bmatrix} \tag{22}$$

$$\boldsymbol{F}_{\mathbf{u}} = \frac{3}{2}\begin{bmatrix} I_{\mathrm{d0}} & I_{\mathrm{q0}} & 0 \\ I_{\mathrm{q0}} & I_{\mathrm{d0}} & 0 \\ 0 & 0 & 0 \end{bmatrix} \tag{23}$$

The *dq*-frame command voltage is expressed as follows:

$$\begin{bmatrix} e_{\mathrm{d}} \\ e_{\mathrm{q}} \end{bmatrix} = \begin{bmatrix} \cos(\delta) & -\sin(\delta) \\ \sin(\delta) & \cos(\delta) \end{bmatrix}\begin{bmatrix} E_{\mathrm{m}} \\ 0 \end{bmatrix} \tag{24}$$

Add the *dq*-frame small-signal disturbances to (24) and eliminate the steady-state value and the secondary disturbance:

$$\begin{bmatrix} \Delta e_{\mathrm{d}} \\ \Delta e_{\mathrm{q}} \end{bmatrix} = \begin{bmatrix} -E_{\mathrm{m}}\sin(\delta_0) & \cos(\delta_0) \\ E_{\mathrm{m}}\cos(\delta_0) & \sin(\delta_0) \end{bmatrix}\begin{bmatrix} \Delta e_{\mathrm{m}} \\ \Delta\theta \end{bmatrix} \tag{25}$$

Then, $\boldsymbol{T}_{\mathbf{I}}$ is defined as follows:

$$\boldsymbol{T}_{\mathbf{I}} = \begin{bmatrix} -E_{\mathrm{m}}\sin(\delta_0) & \cos(\delta_0) & 0 \\ E_{\mathrm{m}}\cos(\delta_0) & \sin(\delta_0) & 0 \\ 0 & 0 & 0 \end{bmatrix} \tag{26}$$

The relationship between the input voltage and the output current can be expressed as follows:

$$\begin{bmatrix} \Delta u_{\mathrm{d}} \\ \Delta u_{\mathrm{q}} \\ \Delta u_{\mathrm{dc}} \end{bmatrix} = -\boldsymbol{Z}_{\mathbf{vsm}}\begin{bmatrix} \Delta i_{\mathrm{d}} \\ \Delta i_{\mathrm{q}} \\ \Delta i_{\mathrm{dc}} \end{bmatrix} \tag{27}$$

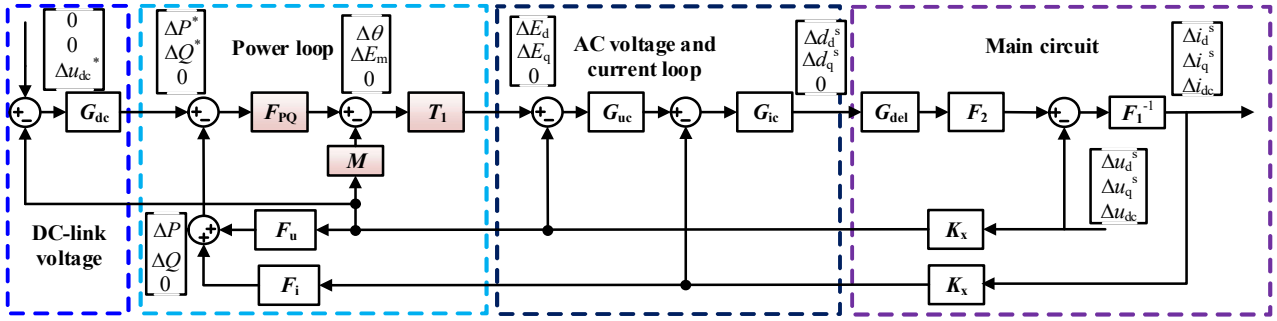

Fig. 2 The wideband dq-frame small-signal model of the VSM.

This article has been accepted for publication in a future issue of this journal, but has not been fully edited. Content may change prior to final publication. Citation information: DOI 10.1109/TIE.2021.3076711, IEEE Transactions on Industrial Electronics

Solving the equations represented by Fig. 2, the hybrid AC/DC impedance of the VSM rectifier is derived as follows:

$$\boldsymbol{Z}_{\text{vsm\_rec}} = \left(\boldsymbol{F}_2\boldsymbol{G}_{\text{del}}\boldsymbol{G}_{\text{ic}}\boldsymbol{G}_{\text{uc}}\left(\boldsymbol{I}+\boldsymbol{T}_1\left(\boldsymbol{M}+\boldsymbol{F}_{\text{PQ}}\left(\boldsymbol{F}_{\text{u}}+\boldsymbol{G}_{\text{dc}}\right)\right)\right)\boldsymbol{K}_{\text{x}}+\boldsymbol{I}\right)^{-1}\cdot \left(\boldsymbol{F}_1+\boldsymbol{F}_2\boldsymbol{G}_{\text{del}}\boldsymbol{G}_{\text{ic}}\left(\boldsymbol{I}+\boldsymbol{G}_{\text{uc}}\boldsymbol{T}_1\boldsymbol{F}_{\text{PQ}}\boldsymbol{F}_{\text{i}}\right)\boldsymbol{K}_{\text{x}}\right) \quad (28)$$

The hybrid AC/DC impedance model of the VSM-based inverter by removing $\mathbf{G}_{\text{dc}}$ of (28) is derived as follows:

$$\boldsymbol{Z}_{\text{vsm\_vsi}} = \left(\boldsymbol{F}_2\boldsymbol{G}_{\text{del}}\boldsymbol{G}_{\text{ic}}\boldsymbol{G}_{\text{uc}}\left(\boldsymbol{I}+\boldsymbol{T}_1\left(\boldsymbol{M}+\boldsymbol{F}_{\text{PQ}}\boldsymbol{F}_{\text{u}}\right)\right)\boldsymbol{K}_{\text{x}}+\boldsymbol{I}\right)^{-1}\cdot \left(\boldsymbol{F}_1+\boldsymbol{F}_2\boldsymbol{G}_{\text{del}}\boldsymbol{G}_{\text{ic}}\left(\boldsymbol{I}+\boldsymbol{G}_{\text{uc}}\boldsymbol{T}_1\boldsymbol{F}_{\text{PQ}}\boldsymbol{F}_{\text{i}}\right)\boldsymbol{K}_{\text{x}}\right) \quad (29)$$

IV. Impedance Comparative Analysis of VSM-Based Rectifier Station and VSM-Based Inverter Station

A. Verification and Characteristics Analysis of Hybrid AC/DC Impedance Model of VSMs

The impedance measurement is the most direct way to verify the impedance models. The simulation measurement results are obtained by MATLAB/Simulink, and the experimental results are obtained by RT_LAB. The measurement method is given in Appendix. When the impedance measurements are carried out by RT_LAB, the serious disturbance voltages adopt ideal voltage sources, and only the controllers of the HVDC system are real. The parameter design of VSMs refers to [4], as shown in Table I. The bandwidth of the current loop, the dc voltage loop, and the synchronization loop are set as 230 Hz, 8Hz, and 16 Hz, respectively. The simulation and experimental measurement results verify the impedance models (Fig. 3 and Fig. 4). Besides, the impedance characteristics of the VSM-based rectifier and inverter are compared as follows:

1) There exists AC/DC coupling in both $\boldsymbol{Z}_{\text{vsm\_rec}}$ and $\boldsymbol{Z}_{\text{vsm\_inv}}$ especially when the dc-link capacitor is small, and the AC/DC

TABLE I
System Parameters of the Inverter Station

Symbol	Description	Value
U_{dc}	DC-link voltage	±100 kV
U_{g}	Grid voltage	90 kV
L_{g1}	Grid-side inductor of the rectifier station	5 mH
L_{g2}	Grid-side inductor of the inverter station	5 mH
S_{n}	Rated capacity	200 MVA
L_{dc}	Inductance of the DC Line	7.9 mH
R_{dc}	Resistance of the DC line	0.6950 Ω
ω_{ic}	Cut-off frequency of sampling filter	10 kHz
ω_{vc}	Cut-off frequency of voltage sampling	10 kHz
C_{dc}	DC-link capacitor of the VSM	5 mF
f_0	Grid frequency	50 Hz
f_{s}	Switch frequency	2 kHz
J_{r}	Virtual moment of inertia of rectifier	1089.8 kg.m^2
D_{pr}	Active damping coefficient of rectifier	326930
L_{v}	Virtual inductance	5 mH
R_{v}	Virtual resistance	0. 2 Ω
K	Integral coefficient	14286
J_{i}	Virtual moment of inertia of the rectifier	5000 kg.m^2
D_{pi}	Active damping gain of the rectifier	254650
D_{q}	Reactive damping gain	325
k_{pu}	Proportional gain of voltage controller	91.5
k_{iu}	Integrator gain of voltage controller	288
k_{p}	Proportional gain of current controller	4.6250e-05
ω_{r}	Cutoff frequency of PR controller	6π
k_{r}	Resonance gain of current controller	0.001

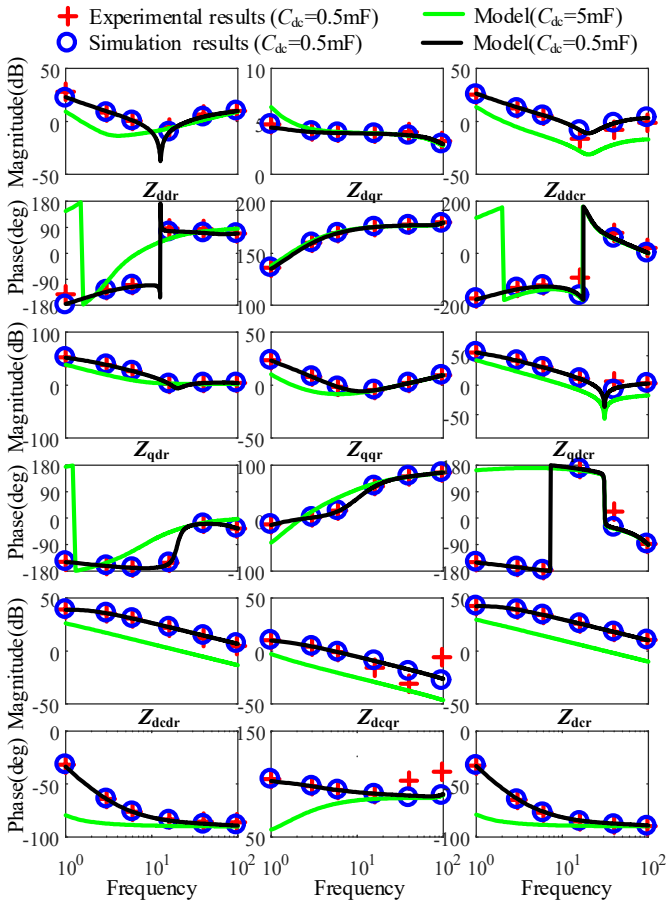

Fig. 3 Hybrid AC/DC impedance of the VSM-based rectifier.

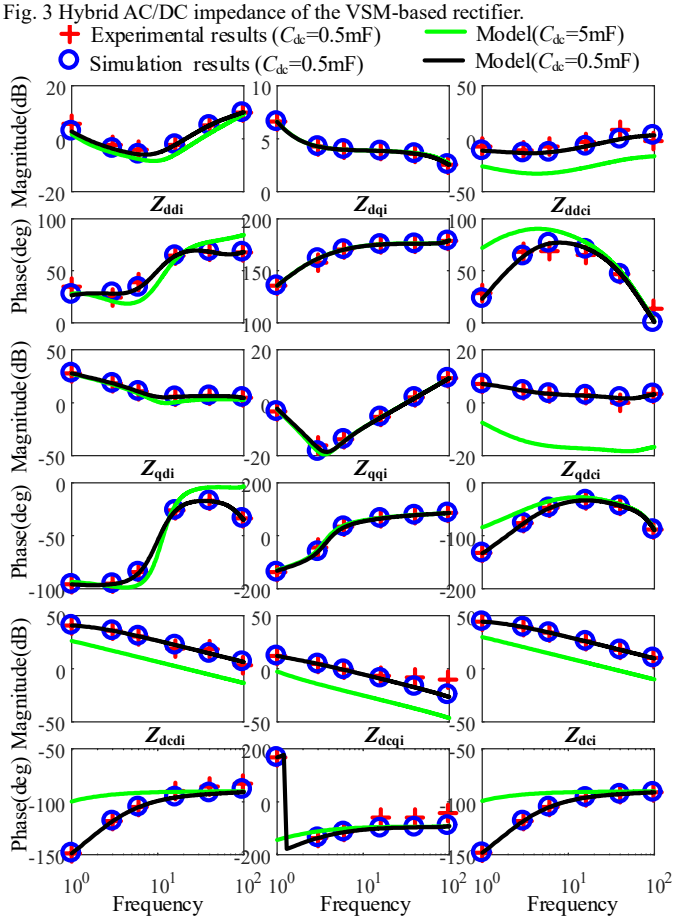

Fig. 4 Hybrid AC/DC impedance of the VSM-based inverter.

coupling of $\boldsymbol{Z}_{\mathbf{vsm\_rec}}$ is stronger than that of $\boldsymbol{Z}_{\mathbf{vsm\_inv}}$ in the low-frequency range. It implies that dc-link voltage controllers enhance the AC/DC coupling of the VSMs. Besides, increasing the dc-link capacitor can weaken the coupling.

2) Z_{dd} of the VSM-based rectifier station behaves as a negative resistor, and its impedance magnitude is V-shaped in the low-frequency range. Besides, Z_{qq} of the VSM-based inverter also behaves as a negative resistor below 2Hz.

B. The Relationship between the Hybrid AC/DC Impedance, DQ-Frame Impedance, and DC Impedance

Both the DC impedance and *dq*-frame impedance can be obtained from the hybrid AC/DC impedance. The hybrid AC/DC impedance of the converter is given by:

$$\begin{bmatrix}\Delta u_{\mathrm{d}}\\ \Delta u_{\mathrm{q}}\\ \Delta u_{\mathrm{dc}}\end{bmatrix}=\begin{bmatrix}Z_{\mathrm{dd}} & Z_{\mathrm{dq}} & Z_{\mathrm{ddc}}\\ Z_{\mathrm{qd}} & Z_{\mathrm{qq}} & Z_{\mathrm{qdc}}\\ Z_{\mathrm{dcd}} & Z_{\mathrm{dcq}} & Z_{\mathrm{dc}}\end{bmatrix}\begin{bmatrix}\Delta i_{\mathrm{d}}\\ \Delta i_{\mathrm{q}}\\ \Delta i_{\mathrm{dc}}\end{bmatrix} \tag{30}$$

The grid-side small-signal dynamics are expressed as

$$\begin{bmatrix}\Delta u_{\mathrm{d}}\\ \Delta u_{\mathrm{q}}\end{bmatrix}=-\boldsymbol{Z}_{\mathbf{g}}\begin{bmatrix}\Delta i_{\mathrm{d}}\\ \Delta i_{\mathrm{q}}\end{bmatrix} \tag{31}$$

Embedding (30) and (31), the relationship between the DC impedance and the hybrid AC/DC impedance is

$$Z_{\mathrm{dcn}}=-\begin{bmatrix}Z_{\mathrm{dcd}} & Z_{\mathrm{dcq}}\end{bmatrix}(Z_{\mathrm{g}}+\begin{bmatrix}Z_{\mathrm{dd}} & Z_{\mathrm{dq}}\\ Z_{\mathrm{qd}} & Z_{\mathrm{qq}}\end{bmatrix})^{-1}\begin{bmatrix}Z_{\mathrm{ddc}}\\ Z_{\mathrm{qdc}}\end{bmatrix}+Z_{\mathrm{dc}} \tag{32}$$

The DC-side small-signal dynamic in the latter stage is

$$\Delta u_{\mathrm{dc}}=-Z_{\mathrm{dcn1}}\Delta i_{\mathrm{dc}} \tag{33}$$

where Z_{dcn1} is the DC impedance of the later-stage converter.

Based on (30) and (33), the relationship between the *dq*-frame impedance and the hybrid AC/DC impedance is

$$\boldsymbol{Z}_{\mathbf{DQ}}=\begin{bmatrix}Z_{\mathrm{dd}} & Z_{\mathrm{dq}}\\ Z_{\mathrm{qd}} & Z_{\mathrm{qq}}\end{bmatrix}-\frac{1}{Z_{\mathrm{dc}}+Z_{\mathrm{dcn1}}}\begin{bmatrix}Z_{\mathrm{ddc}}Z_{\mathrm{dcd}} & Z_{\mathrm{ddc}}Z_{\mathrm{dcq}}\\ Z_{\mathrm{qdc}}Z_{\mathrm{dcd}} & Z_{\mathrm{qdc}}Z_{\mathrm{dcq}}\end{bmatrix} \tag{34}$$

C. Comparative Analysis of DQ-Frame Impedances

The *dq*-frame impedance of the VSM-based rectifier station according to (28) and (34) is expressed as follows:

$$\boldsymbol{Z}_{\mathbf{dqrec}}=\begin{bmatrix}Z_{\mathrm{ddr}} & Z_{\mathrm{dqr}}\\ Z_{\mathrm{qdr}} & Z_{\mathrm{qqr}}\end{bmatrix}-\frac{1}{Z_{\mathrm{dcr}}+Z_{\mathrm{dcinv}}+Z_{\mathrm{li}}}\begin{bmatrix}Z_{\mathrm{ddcr}}Z_{\mathrm{dcdr}} & Z_{\mathrm{ddcr}}Z_{\mathrm{dcqr}}\\ Z_{\mathrm{qdcr}}Z_{\mathrm{dcdr}} & Z_{\mathrm{qdcr}}Z_{\mathrm{dcqr}}\end{bmatrix} \tag{35}$$

The *dq*-frame impedance of the VSM-based inverter station according to (29) and (34) is expressed as follows:

$$\boldsymbol{Z}_{\mathbf{dqinv}}=\begin{bmatrix}Z_{\mathrm{ddi}} & Z_{\mathrm{dqi}}\\ Z_{\mathrm{qdi}} & Z_{\mathrm{qqi}}\end{bmatrix}-\frac{1}{Z_{\mathrm{dci}}+Z_{\mathrm{dcrec}}+Z_{\mathrm{li}}}\begin{bmatrix}Z_{\mathrm{ddci}}Z_{\mathrm{dcdi}} & Z_{\mathrm{ddci}}Z_{\mathrm{dcqi}}\\ Z_{\mathrm{qdci}}Z_{\mathrm{dcdi}} & Z_{\mathrm{qdci}}Z_{\mathrm{dcqi}}\end{bmatrix} \tag{36}$$

$\boldsymbol{Z}_{\mathbf{dqrec1}}$ denotes the *dq*-frame impedance of the VSM-based rectifier regarding the dc side as a constant resistor. $\boldsymbol{Z}_{\mathbf{dqinv1}}$ denotes the *dq*-frame impedance of the VSM-based inverter regarding the dc side as a constant value. The sweep results verify the accuracy of the theoretical $\boldsymbol{Z}_{\mathbf{dqrec}}$ and $\boldsymbol{Z}_{\mathbf{dqinv}}$ (Fig. 5 and Fig. 6). Figure 5 shows that the dc-link dynamics of the inverter station have great impacts on the *dq*-frame impedance of the rectifier station in the low-frequency range. Figure 6 shows that the dc-link dynamics of the rectifier also have impacts on the *dq*-frame impedance of the inverter especially when the dc-link capacitor is small.

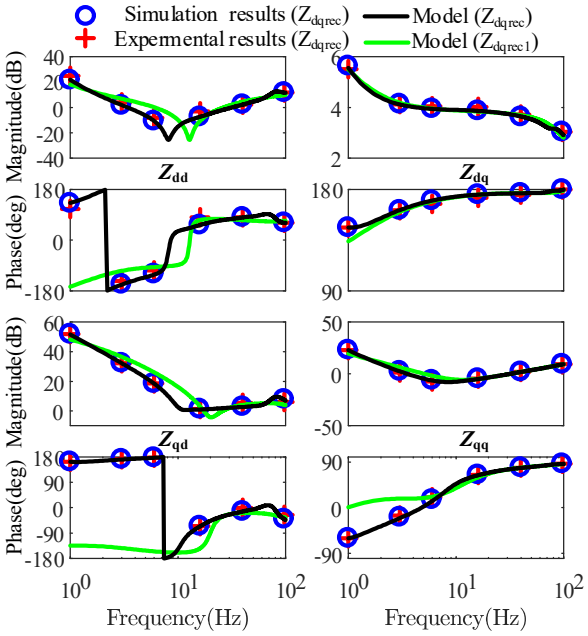

Fig. 5 The *dq*-frame impedance of the VSM-based rectifier station.

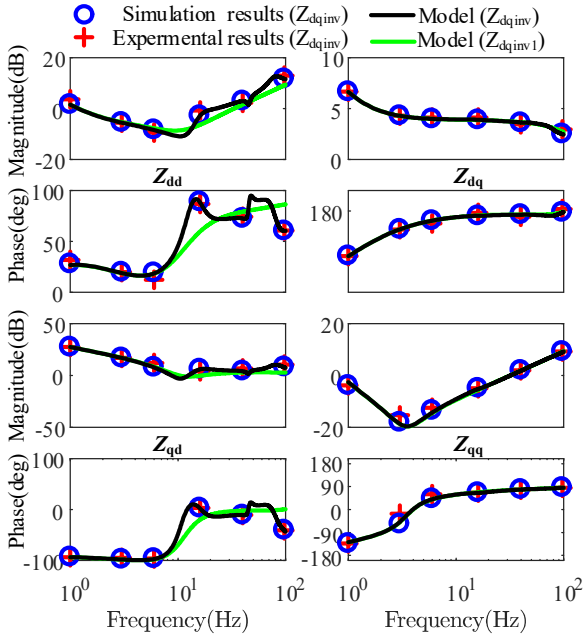

Fig. 6 The *dq*-frame impedance of the VSM-based inverter station.

D. Comparative Analysis of DC Impedances

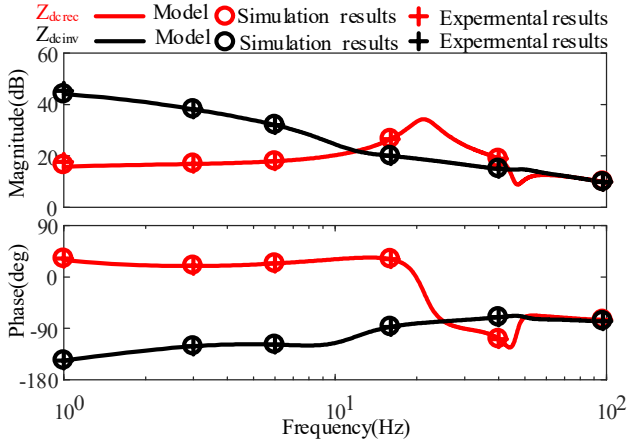

Fig. 7 DC impedance of the VSM-based rectifier station and inverter station.

TABLE II
IMPEDANCE COMPARISON OF THE VSM RECTIFIER AND VSM INVERTER: DC IMPEDANCE, DQ IMPEDANCE, AND HYBRID AC/DC IMPEDANCE

	DC impedance		DQ impedance		Hybrid AC/DC impedance	
	VSM Rectifier	VSM Inverter	VSM Rectifier	VSM Inverter	VSM Inverter	VSM Inverter
Dimension	1	1	2	2	3	3
Behave negative resistors in the low-frequency range	Yes	No	Z_{dd}	Z_{qq}	Z_{ddr}	Z_{qqi} and Z_{dci}
If influenced by the AC grid	Yes	Yes	Yes	Yes	No	No
If influenced by the other converter	Yes	Yes	Yes	Yes	No	No
If possibly contain RHP poles	Yes	Yes	Yes	Yes	No	No

Z_{dcrec} that denotes the DC impedance of the VSM-based rectifier station is obtained according to (28) and (34). Z_{dcinv} that denotes the DC impedance of the VSM-based inverter station is obtained according to (29) and (34). The measurement results are consistent with the theoretical models, which verifies the accuracy of the models (Fig. 7).

Z_{dcinv} shows negative resistance characteristics and is easy to intersect with Z_{dcrec} in the low-frequency range. It means that the low-frequency oscillation could occur due to the DC-side interaction between the VSM-based rectifier station and the inverter station. As compared in Table II, the DC impedance of the converter contains the information of the grid, and the *dq*-frame impedance contains the information of the converter in the later stage. By comparison, the hybrid AC/DC impedance only includes the information of the converter. Thus, the stability analysis based on the DC or *dq*-frame impedances needs to calculate RHP poles or zeros that cannot be obtained in the actual system, which makes the analysis results incorrect.

V. SYSTEM STABILITY ANALYSIS BASED ON THE FIVE-DIMENSION IMPEDANCE STABILITY CRITERION

A. Five-Dimension Impedance Stability Criterion

The five dimension stability criterion based on the hybrid AC/DC impedances is derived below.

The equivalent model of the HVDC system is shown in Fig. 1(b), and two AC grid-side circuits are described as follows:

$$\begin{bmatrix}\Delta i_{d1}\\ \Delta i_{q1}\end{bmatrix} = \boldsymbol{Z}_{\mathbf{g1}}^{-1}\left(\begin{bmatrix}\Delta u_{gd1}\\ \Delta u_{gq1}\end{bmatrix} - \begin{bmatrix}\Delta u_{d1}\\ \Delta u_{q1}\end{bmatrix}\right) \tag{37}$$

$$\begin{bmatrix}\Delta i_{d2}\\ \Delta i_{q2}\end{bmatrix} = \boldsymbol{Z}_{\mathbf{g2}}^{-1}\left(\begin{bmatrix}\Delta u_{gd2}\\ \Delta u_{gq2}\end{bmatrix} - \begin{bmatrix}\Delta u_{d2}\\ \Delta u_{q2}\end{bmatrix}\right) \tag{38}$$

where $\boldsymbol{Z}_{\mathbf{g1}}$ and $\boldsymbol{Z}_{\mathbf{g2}}$ represent the grid impedance of the rectifier station and inverter station in the *dq* frame, respectively.

The DC-side passive network can be expressed as follows:

$$\Delta i_{dc1} = -\Delta i_{dc2} = -\frac{\Delta u_{dc1} - \Delta u_{dc2}}{2\left(L_{dc}s + R_{dc}\right)} \tag{39}$$

Based on (37)-(39), the variables of the AC grids and DC parts can be modeled together by

$$\begin{bmatrix}\Delta i_{d1}\\ \Delta i_{q1}\\ \Delta i_{dc1}\\ \Delta i_{d2}\\ \Delta i_{q2}\end{bmatrix} = \boldsymbol{Y}_{\mathbf{acdcnet}}\left(\begin{bmatrix}\Delta u_{gd1}\\ \Delta u_{gq1}\\ 0\\ \Delta u_{gd2}\\ \Delta u_{gq2}\end{bmatrix} - \begin{bmatrix}\Delta u_{d1}\\ \Delta u_{q1}\\ \Delta u_{dc1} - \Delta u_{dc2}\\ \Delta u_{d2}\\ \Delta u_{q2}\end{bmatrix}\right) \tag{40}$$

where $\boldsymbol{Y}_{\mathbf{acdcnet}}$ is defined as follows:

$$\boldsymbol{Y}_{\mathbf{acdcnet}} = \begin{bmatrix}\boldsymbol{Z}_{\mathbf{g1}}^{-1} & 0 & 0 & 0\\ & 0 & 0 & 0\\ 0 \quad 0 & \dfrac{1}{2(L_{dc}s + R_{dc})} & 0 & 0\\ 0 & 0 & 0 & \boldsymbol{Z}_{\mathbf{g2}}^{-1}\\ 0 & 0 & 0 & \end{bmatrix} \tag{41}$$

Meantime, according to (30) and (39), the small-signal voltages and currents of the AC/DC ports of the HVDC rectifier and inverter station can be expressed as follows:

$$\begin{bmatrix}\Delta u_{d1}\\ \Delta u_{q1}\\ \Delta u_{dc1} - \Delta u_{dc2}\\ \Delta u_{d2}\\ \Delta u_{q2}\end{bmatrix} = \boldsymbol{Z}_{\mathbf{vsmacdc}}\begin{bmatrix}\Delta i_{d1}\\ \Delta i_{q1}\\ \Delta i_{dc1}\\ \Delta i_{d2}\\ \Delta i_{q2}\end{bmatrix} \tag{42}$$

where $\boldsymbol{Z}_{\mathbf{vsmacdc}}$ is defined as follows:

$$\boldsymbol{Z}_{\mathbf{vsmacdc}} = \begin{bmatrix}Z_{ddr} & Z_{dqr} & Z_{ddcr} & 0 & 0\\ Z_{qdr} & Z_{qqr} & Z_{qdcr} & 0 & 0\\ Z_{dcdr} & Z_{dcqr} & Z_{dcr}+Z_{dci} & -Z_{dcdi} & -Z_{dcqi}\\ 0 & 0 & -Z_{ddci} & Z_{ddi} & Z_{dqi}\\ 0 & 0 & -Z_{qdci} & Z_{qdi} & Z_{qqi}\end{bmatrix} \tag{43}$$

The DC and AC-side currents of the VSC-HVDC system are derived according to (40) and (42) as follows:

$$\begin{bmatrix}\Delta i_{d1}\\ \Delta i_{q1}\\ \Delta i_{dc1}\\ \Delta i_{d2}\\ \Delta i_{q2}\end{bmatrix} = \left(\boldsymbol{I} + \boldsymbol{Y}_{\mathbf{acdcnet}}\boldsymbol{Z}_{\mathbf{vsmacdc}}\right)^{-1}\boldsymbol{Y}_{\mathbf{acdcnet}}\begin{bmatrix}\Delta u_{gd1}\\ \Delta u_{gq1}\\ 0\\ \Delta u_{gd2}\\ \Delta u_{gq2}\end{bmatrix} \tag{44}$$

The system minor loop gain based on (44) is defined as follows:

$$L(s) = \boldsymbol{Y}_{\mathbf{acdcnet}}\boldsymbol{Z}_{\mathbf{vsmacdc}} \tag{45}$$

Based on GINC, the system stability depends on the Nyquist diagram and the number of the RHP zeros [25]. Since both converters are designed to be stable when they operate standalone, $\boldsymbol{Z}_{\mathbf{vsmacdc}}$ and $\boldsymbol{Y}_{\mathbf{acdcnet}}$ contain no RHP zeros. Thus, the stability of the HVDC system is assessed by judging whether the inverse characteristic loci of L(s) encircles (-1, 0) point or not. Besides, the frequency where the inverse characteristic loci intersect the unit circle is the predictive oscillation frequency of the system in the dq frame. The advantages of the proposed criterion are that RHP poles or zeros of the system impedance

This article has been accepted for publication in a future issue of this journal, but has not been fully edited. Content may change prior to final publication. Citation information: DOI 10.1109/TIE.2021.3076711, IEEE Transactions on Industrial Electronics

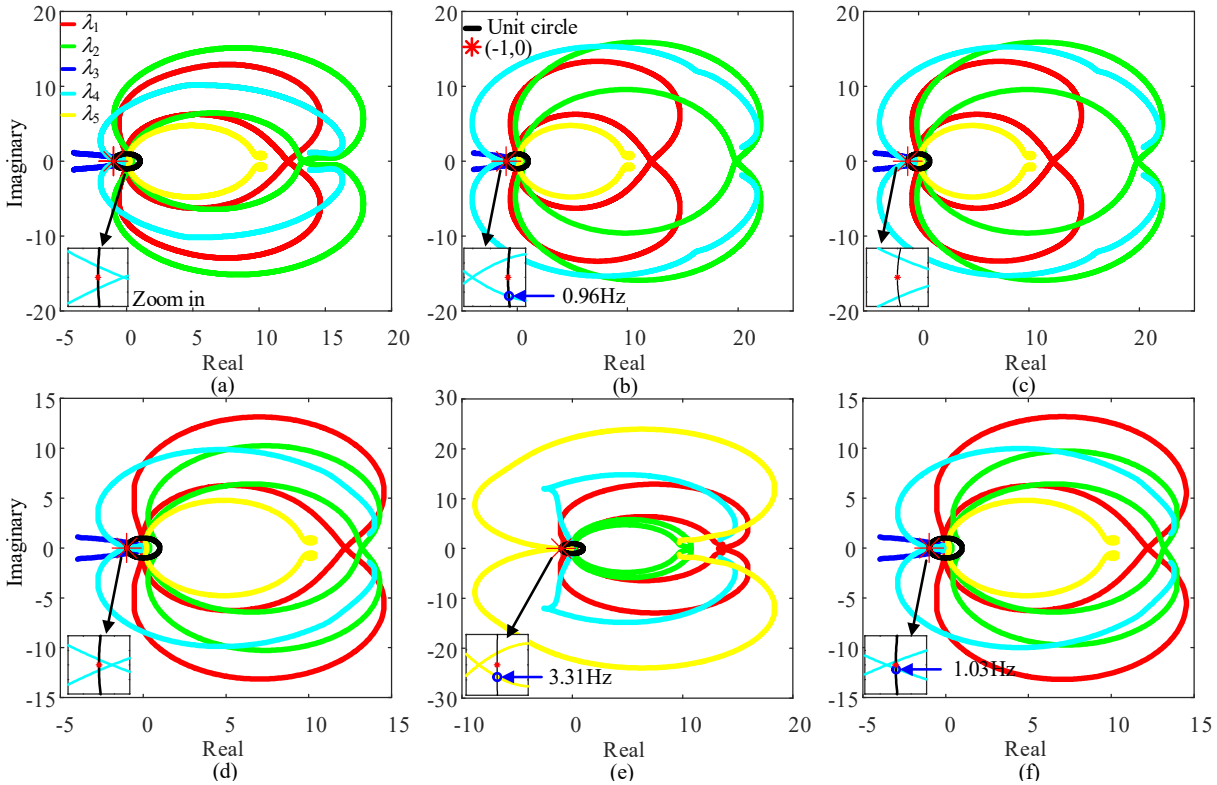

Fig. 8 Inverse characteristic loci of $L(s)$, SCRi=4. (a) SCRr=3, k_{ui}=288, D_p=326929, C_{dc}=5 mF; (b) SCRr=2, k_{ui}=288, D_p=326929, C_{dc}=5 mF; (c) SCR=2, k_{ui}=144, D_p=326929, C_{dc}=5 mF; (d) SCRr=3, k_{ui}=288, D_p=490390, C_{dc}=5 mF; (e) SCRr=3, k_{ui}=288, D_p=490390, C_{dc}=0.5 mF; (f) SCRr=3, k_{ui}=288, D_p=523090, C_{dc}=5 mF.

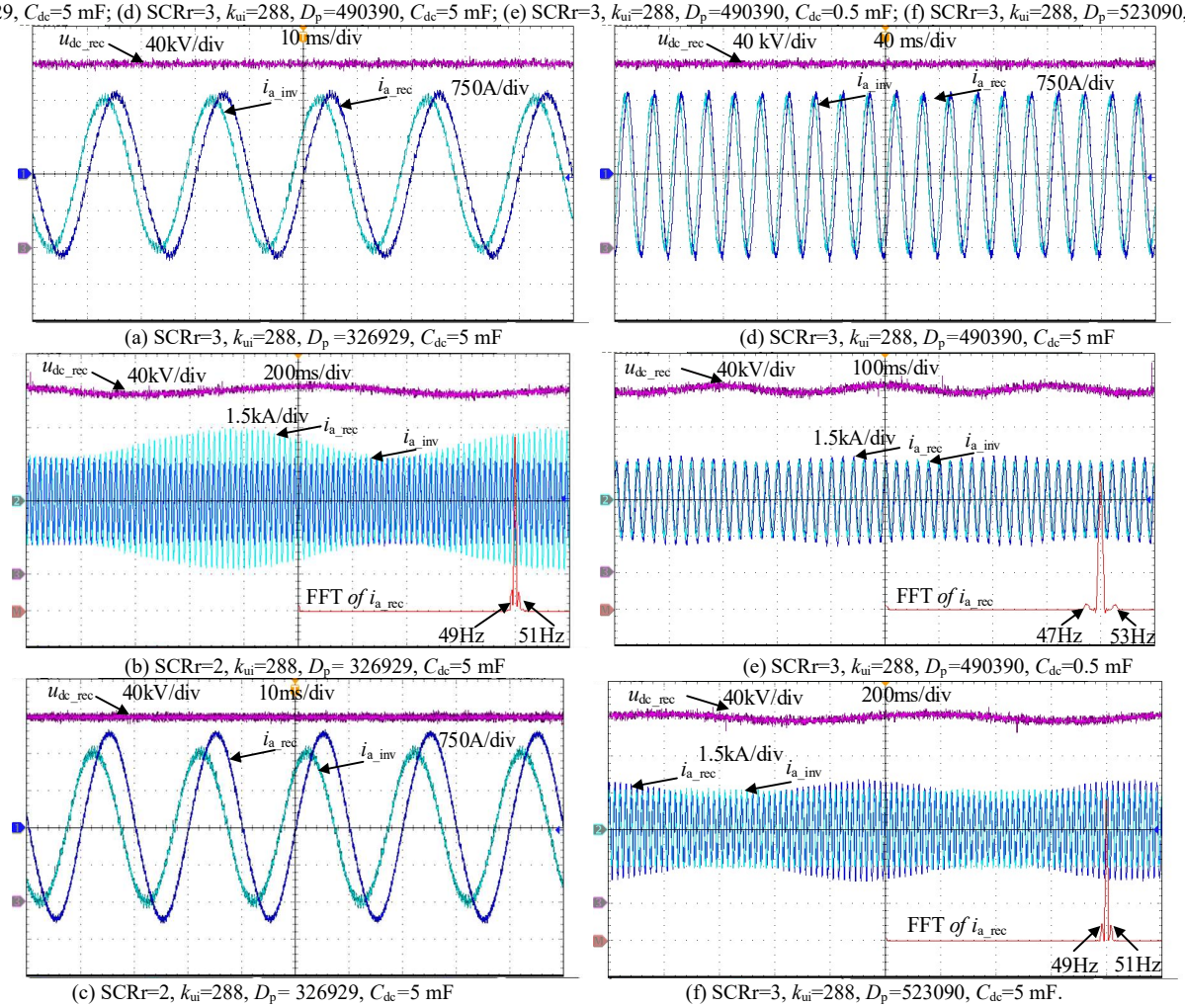

(a) SCRr=3, k_{ui}=288, D_p =326929, C_{dc}=5 mF

(d) SCRr=3, k_{ui}=288, D_p=490390, C_{dc}=5 mF

(b) SCRr=2, k_{ui}=288, D_p= 326929, C_{dc}=5 mF

(e) SCRr=3, k_{ui}=288, D_p=490390, C_{dc}=0.5 mF

(c) SCRr=2, k_{ui}=288, D_p= 326929, C_{dc}=5 mF

(f) SCRr=3, k_{ui}=288, D_p=523090, C_{dc}=5 mF.

Fig. 9 Experimental results based on the RT-LAB corresponding to the stability analyses in Fig. 8, SCRi=4.

This article has been accepted for publication in a future issue of this journal, but has not been fully edited. Content may change prior to final publication. Citation information: DOI 10.1109/TIE.2021.3076711, IEEE Transactions on Industrial Electronics

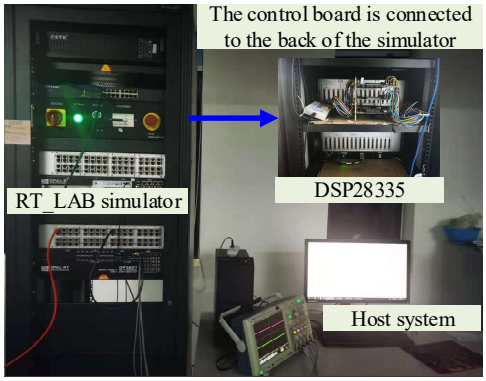

Fig. 10 Experimental system based on RT_LAB.

ratio don't need to be calculated, and it has a relatively small computation and a wider range of applications. The shortcoming is that the instability mechanism cannot be directly observed by the impedance bode plot, due to the strong coupling among the d, q, and dc frames.

B. Stability Analysis and Experimental Results

To further verify the correctness of the theoretical analysis, experiments have been carried out on the hardware-in-the-loop experimental platform, as shown in Fig. 10. The experimental parameters are the same as those of the previous simulation. The VSM-based rectifier station and inverter station are controlled by TI DSP TMS320F28335 through the I/O interface of the RT_LAB. The other parts of the HVDC system such as the main circuit of the rectifier station and the inverter station are simulated in FPGA and the program is implemented in CPU.

All characteristic loci of $L(s)$ are obtained by MATLAB, and the reciprocals of characteristic loci are plotted in Fig. 8 after the implementation of the sort program. Each Nyquist diagram shown in Fig. 8 is supposed to have five curves.

As shown in Fig.8 (a), all inverse characteristic loci do not encircle (-1, 0) when SCR=3, meaning that the HVDC system is stable. It is verified by the experimental results in Fig. 9 (a). Compared with Fig. 8(a), Fig. 8 (b) shows that one inverse characteristic locus encircles (-1, 0) when SCR=2, and it intersects with the unit cycle at 0.96 Hz. It means that the oscillation with 0.96 Hz will occur in the dq frame, corresponding to 50 Hz±0.96 Hz in the *abc* frame. It is verified by experimental results in Fig. 9 (b), where the DFT analysis of i_{a_rec} shows two main resonant components at 50±1 Hz. Compared with Fig. 8 (b), Fig. 8(c) shows that all inverse characteristic loci do not encircle (-1, 0) only when the integral coefficient (k_{ip}) of the VSM rectifier decreases from 288 to 144, meaning that decreasing the k_{ip} enhances the stability of HVDC system. It is verified by the experimental results in Fig. 9 (c).

Compared with Fig.8 (d), Fig.8 (e) shows that one inverse characteristic locus encircles (-1, 0) with decreasing the dc-link capacitor (C_{dc}) of the VSM, and it intersects with the unit cycle at 3.3Hz, meaning that decreasing C_{dc} destabilizes the system. It is verified by experimental results in Fig. 9 (d) and Fig. 9 (e), where the system becomes unstable after only changing C_{dc} from 5mH to 0.5mH. Besides, Fig. 9 (e) shows that the DFT analysis of i_{a_rec} shows two main resonant components at 50±3Hz, which is approximately consistent with the predictive value (50±3.3Hz).

Compared with Fig. 8(d), Fig. 8(f) shows that one inverse characteristic locus gradually encircles (-1, 0) with increasing the damping coefficient (D_{pr}) of the VSM-based rectifier, meaning that increasing D_{pr} destabilizes the system. It is verified by the experimental results in Fig. 9(d) and Fig. 9(e), where the system becomes unstable after only increasing D_{pr}. Besides, the DFT analysis of i_{a_rec} shows two main resonant components at 50±1Hz, which is consistent with the predictive value (50±1.03 Hz). The experimental results in Fig. 9 further verify the effectiveness of the stability criterion. Besides, It is found that increasing the integral gain of the dc-link voltage controller and the damping coefficient or decreasing the dc-link capacitor of the VSM rectifier destabilizes the system.

VI. Conclusions

This paper aims to assess the stability of the VSM-based HVDC systems, and the established hybrid AC/DC impedance models of the VSMs and the five-dimension impedance stability criterion has been verified by experimental results. Some conclusions were drawn:

1) The accurate hybrid AC/DC impedance models of the VSM-based rectifier station and inverter station have been established and verified by the improved measurement method.

2) The DC impedance of the VSM-based inverter station behaves as the negative resistor in the low-frequency range.

3) A five-dimension impedance stability criterion based on the GINC and the hybrid AC/DC impedance has been proposed to accurately analyze the point-to-point VSC-HVDC system.

4) The d-d channel negative resistor behavior of the VSM-based rectifier station could induce low-frequency oscillations when the grid SCR is small. Decreasing the integral coefficient of the dc-link voltage controller and the damping coefficient, and increasing the dc-link capacitor of the VSM rectifier can enhance the system stability.

Appendix

The hybrid AC/DC impedance, dc impedance, and dq-frame impedance of the three-phase converter can be measured together, as shown in Fig. 11. At first, three linear independent series voltages are injected. Then, the dq-frame and dc-link voltages and currents are collected. Appling FFT to the sample signals, the hybrid AC/DC impedance is calculated as follows:

$$\boldsymbol{Z}_{\mathbf{ad}} = \begin{bmatrix} U_{d1} & U_{d2} & U_{d3} \\ U_{q1} & U_{q2} & U_{q3} \\ U_{dc1} & U_{dc2} & U_{dc3} \end{bmatrix} \begin{bmatrix} I_{d1} & I_{d2} & I_{d3} \\ I_{q1} & I_{q2} & I_{q3} \\ I_{dc1} & I_{dc2} & I_{dc3} \end{bmatrix}^{-1} \tag{46}$$

The PLL used for the impedance measurement has great impacts on the hybrid AC/DC impedance measurement, especially during the PLL bandwidth. Thus, after mitigating the PLL dynamics, the actual impedance $\mathbf{Z}_{\mathbf{acdc}}$ is

$$\boldsymbol{Z}_{\mathbf{acdc}} = \left(\boldsymbol{Z}_{\mathbf{ad}}^{-1} \begin{bmatrix} 1 & U_{q0}G_{pll} & 0 \\ 0 & 1-U_{d0}G_{pll} & 0 \\ 0 & 0 & 1 \end{bmatrix} - \begin{bmatrix} 0 & I_{q0}G_{pll} & 0 \\ 0 & -I_{d0}G_{pll} & 0 \\ 0 & 0 & 0 \end{bmatrix} \right)^{-1} \tag{47}$$

G_{pll} is expressed as follows:

$$G_{pll}=(k_{ppll} + k_{ipll}/s)/(s+U_{d0}(k_{ppll} + k_{ipll}/s)) \tag{48}$$

where k_{ppll} and k_{ipll} are PI gains of the PLL, respectively.

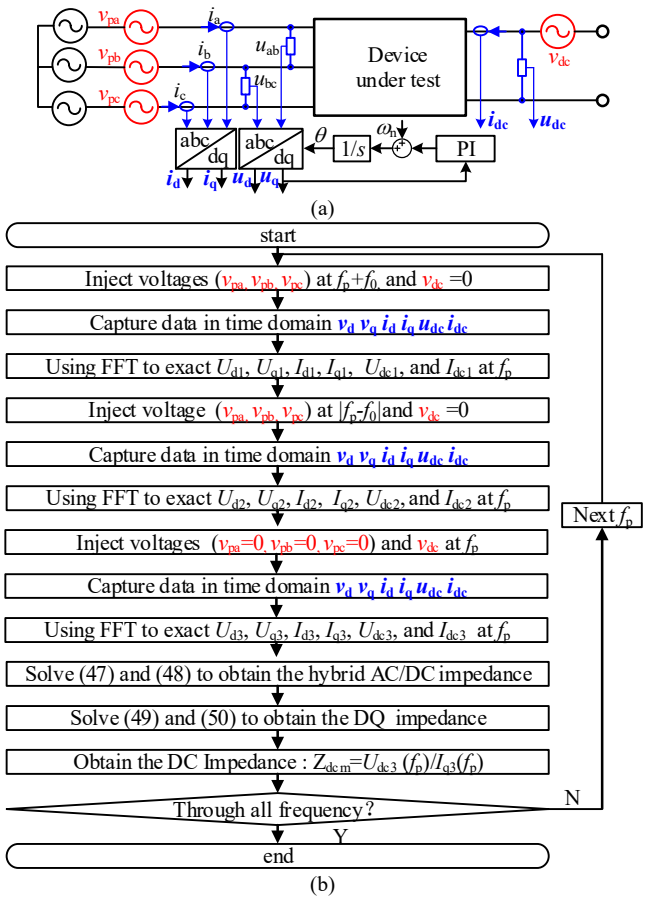

Fig. 11 Impedance measurement method. (a) The measurement circuit; (b) The measurement method.

Likewise, the dq-frame impedance is calculated as [28]:

$$\boldsymbol{Z}_{\mathbf{dq}}=\begin{bmatrix}U_{d1} & U_{d2}\\ U_{q1} & U_{q2}\end{bmatrix}\begin{bmatrix}I_{d1} & I_{d2}\\ I_{q1} & I_{q2}\end{bmatrix}^{-1} \tag{49}$$

$$\boldsymbol{Z}_{\mathbf{dqm}}=\left(\boldsymbol{Z}_{\mathbf{dq}}^{-1}\begin{bmatrix}1 & U_{q0}G_{pll}\\ 0 & 1-U_{d0}G_{pll}\end{bmatrix}-\begin{bmatrix}1 & I_{q0}G_{pll}\\ 0 & -I_{d0}G_{pll}\end{bmatrix}\right)^{-1} \tag{50}$$

REFERENCES

[1] N. Flourentzou, V. G. Agelidis, and G. D. Demetriades, "VSC-based HVDC power transmission systems: An overview," *IEEE Trans. Power Electron.*, vol. 24, no. 3, pp. 592–602, 2009.

[2] L. P. Kunjumuhammed, B. C. Pal, R. Gupta, and K. J. Dyke, "Stability Analysis of a PMSG-Based Large Offshore Wind Farm Connected to a VSC-HVDC," *IEEE Trans. Energy Convers.*, vol. 32, no. 3, pp. 1166-1176, Sept. 2017.

[3] Q. Zhong and G. Weiss, "Synchronverters: Inverters That Mimic Synchronous Generators," *IEEE Trans. Ind. Electron.*, vol. 58, no. 4, pp. 1259-1267, Apr. 2011.

[4] B. Gao, C. Xia, L. Zhang, and N. Chen, "Modeling and Parameters Design for Rectifier Side of VSC-HVDC Based on Virtual Synchronous Machine Technology," *Proc. of the CSEE*, vol. 37, no. 2, pp. 534–543, Jan. 2017.

[5] Z. Ma, Q. Zhong, and J. D. Yan, "Synchronverter-based Control Strategies for Three-phase PWM Rectifiers," *2012 7th IEEE Conference on Industrial Electronics and Applications (ICIEA)*, Singapore, 2012, pp. 225-230.

[6] L. Huang, H. Xin, and Z. Wang, "Damping Low-Frequency Oscillations Through VSC-HVDC Stations Operated as Virtual Synchronous Machines," *IEEE Trans. Power Electron.*, vol. 34, no. 6, pp. 5803-5818, Jun. 2019.

[7] G. Stamatiou and M. Bongiorno, "Stability Analysis of Two-Terminal VSC-HVDC Systems Using the Net-Damping Criterion," *IEEE Trans. Power Deliv.*, vol. 31, no. 4, pp. 1748-1756, Aug. 2016.

[8] Y. Wang, X. Wang, F. Blaabjerg, and Z. Chen, "Harmonic instability assessment using state-space modeling and participation analysis in inverter-fed power systems," *IEEE Trans. Ind. Electron.*, vol. 64, no. 1, pp. 806–816, Jan 2017.

[9] R. D. Middlebrook, "Input filter considerations in design and application of switching regulators," *in Proc. IEEE Ind. Appl. Soc. Conf.*, Oct. 1976, pp. 94–107.

[10] M. Amin, M. Molinas, J. Lyu, and X. Cai, "Impact of power flow direction on the stability of VSC-HVDC seen from the impedance Nyquist plot," *IEEE Trans. Power Electron.*, vol. 32, no. 10, pp. 8204–8217, 2017.

[11] L. Xu, L. Fan, and Z. Miao, "DC impedance-model-based resonance analysis of a VSC–HVDC system," *IEEE Trans. Power Deliv.*, vol. 30, no. 3, pp. 1221–1230, 2015.

[12] Z. Li et al., "Accurate Impedance Modeling and Control Strategy for Improving the Stability of DC System in Multi-terminal MMC-Based DC Grid," *IEEE Trans. Power Electron.*, vol. 35, no. 10, pp. 10026-10049, Oct. 2020.

[13] G. Pinares and M. Bongiorno, "Modeling and analysis of VSC-based HVDC systems for DC network stability studies," *IEEE Trans. Power Deliv.*, vol. 31, no. 2, pp. 848–856, 2016.

[14] D. Xue, J. Liu, Z. Liu, Y. Tu, and T. Liu, "Modeling and Analysis of DC Terminal Impedance of Voltage-Source Converters With Different Control Modes," *IEEE Trans. Power Electron.*, vol. 35, no. 6, pp. 5883-5896, Jun. 2020.

[15] M. Cespedes and J. Sun, "Impedance Modeling and Analysis of Grid-Connected Voltage-Source Converters," *IEEE Trans. Power Electron.*, vol. 29, no. 3, pp. 1254-1261, Mar. 2014.

[16] B. Wen, D. Boroyevich, R. Burgos, P. Mattavelli, and Z. Shen, "Analysis of D-Q Small-Signal Impedance of Grid-Tied Inverters," *IEEE Trans. Power Electron.*, vol. 31, no. 1, pp. 675-687, Jan. 2016.

[17] C. Zou, H. Rao, S. Xu, et al., "Analysis of Resonance between a VSC-HVDC Converter and the AC Grid," *IEEE Trans. Power Electron.*, vol. 33, no. 12, pp. 10157-10168, Dec. 2018.

[18] W. Wu, Y. Chen, L. Zhou, et al., "Sequence Impedance Modeling and Stability Comparative Analysis of Voltage-Controlled VSGs and Current-Controlled VSGs," *IEEE Trans. Power Electron.*, vol. 66, no. 8, pp. 6460-6472, Aug. 2019.

[19] J. Guo et al., "Wideband dq-frame Impedance Modeling of Load-side Virtual Synchronous Machine and Its Stability Analysis in Comparison With Conventional PWM Rectifier in Weak Grid," *IEEE J. Emerg. Sel. Top. Power Electron.*, early access.

[20] Y. Song and C. Breitholtz, "Nyquist stability analysis of an AC-grid connected VSC-HVDC system using a distributed parameter DC cable model," *IEEE Trans. Power Deliv.*, vol. 31, no. 2, pp. 898–907, 2016.

[21] S. Shah and L. Parsa, "Impedance Modeling of Three-Phase Voltage Source Converters in DQ, Sequence, and Phasor Domains," *IEEE Trans. Energy Convers.*, vol. 32, no. 3, pp. 1139-1150, Sept. 2017.

[22] K. Ji et al., "Generalized Impedance Analysis and New Sight at Damping Controls for Wind Farm Connected MMC-HVDC," *IEEE J. Emerg. Sel. Top. Power Electron.*, early access.

[23] H. Zhang, M. Mehrabankhomartash, M. Saeedifard, Y. Zou, Y. Meng, and X. Wang, "Impedance Analysis and Stabilization of Point-to-Point HVDC Systems based on a Hybrid AC/DC Impedance Model," *IEEE Trans. Ind. Electron.*, early access.

[24] J. Pedra, L. Sainz, and L. Monjo, "Three-Port Small Signal Admittance-Based Model of VSCs for Studies of Multi-terminal HVDC Hybrid AC/DC Transmission Grids," *IEEE Trans. Power Syst.*, early access.

[25] B. Wen, D. Boroyevich, R. Burgos, P. Mattavelli, and Z. Shen, "Inverse Nyquist Stability Criterion for Grid-Tied Inverters," *IEEE Trans. Power Electron.*, vol. 32, no. 2, pp. 1548-1556, Feb. 2017.

[26] M. Amin and M. Molinas, "A Gray-Box Method for Stability and Controller Parameter Estimation in HVDC-Connected Wind Farms Based on Nonparametric Impedance," *IEEE Trans. Ind. Electron.*, vol. 66, no. 3, pp. 1872-1882, Mar. 2019.

[27] O. Mo, S. D'Arco and J. A. Suul, "Evaluation of Virtual Synchronous Machines with Dynamic or Quasi-Stationary Machine Models," *IEEE Trans. Ind. Electron.*, vol. 64, no. 7, pp. 5952-5962, Jul. 2017.

[28] H. Gong, D. Yang, and X. Wang, "Impact Analysis and Mitigation of Synchronization Dynamics for DQ Impedance Measurement," *IEEE Trans. Power Electron.*, vol. 34, no. 9, pp. 8797-8807, Sept. 2019.

[29] D. N. Zmood, D. G. Holmes, and G. H. Bode, "Frequency-domain analysis of three-phase linear current regulators," *IEEE Trans. Ind. Appl.*, vol. 37, no. 2, pp. 601–610, Apr. 2001.

This article has been accepted for publication in a future issue of this journal, but has not been fully edited. Content may change prior to final publication. Citation information: DOI 10.1109/TIE.2021.3076711, IEEE Transactions on Industrial Electronics

Jian Guo was born in Hubei, China, 1995. he received the B.S. degree in electronic information engineering from China University of Mining and Technology, xuzhou, China, in 2017. Currently, he has been working toward the Ph.D. degree in electrical engineering from Hunan University, Changsha, China.

Her research interests include power electronics converter, distributed generation.

Yandong Chen (S'13-M'14-SM'18) was born in Hunan, China, in 1979. He received the B.S. and M.S. degree in instrument science and technology from Hunan University, Changsha, China, in 2003 and 2006, respectively, and the Ph.D. degree in electrical engineering from Hunan University, Changsha, China, in 2014. He is currently a Professor in the College of Electrical and Information Engineering, Hunan University, Changsha. His research interests include power electronics for microgrid, distributed generation, power supply, and energy storage. Dr. Chen is a recipient of the 2014 National Technological Invention Awards of China, and the 2014 WIPO-SIPO Award for Chinese Outstanding Patented Invention. He is a Senior Member of IEEE PES & PELS.

Shuhan Liao (S'18-M'20) was born in Xiangtan, Hunan Province, China, in 1993. She received B. Eng. egree and the Ph. D Degree in electrical engineering from Wuhan University, Wuhan, China, in 2015 and 2020, respectively. From Oct. 2018 to Oct. 2019, she was a guest Ph. D. student with the Department of Energy Technology, Aalborg University, Aalborg, Denmark.

She is currently a Postdoctoral Researcher at Hunan University, Changsha, China. Her main research interests include the modeling and dynamic analysis of renewable energy generation systems.

Wenhua Wu (S'16-M'20) was born in Hunan, China, in 1991. He received the B.S. and Ph.D. degrees in electrical engineering from Hunan University, Changsha, China, in 2014 and 2019, respectively. He is currently a Postdoctoral Researcher in electrical engineering with Hunan University. His research interests include power electronics, modeling, and control of renewable power generation systems.

Xiangyu Wang was born in Hunan, China, 1995. She received the B.S. degree from the College of Electrical and Information Engineering, Central South University, Changsha, China, in 2017. She is currently working toward the M. Eng. Degree with the College of Electrical and Information Engineering, Hunan University, Changsha, China. Her research interests include power electronics converter, distributed generation.

Josep M. Guerrero (S'01-M'04-SM'08-F'15) received the B.S. degree in telecommunications engineering, the M.S. degree in electronics engineering, and the Ph.D. degree in power electronics from the Technical University of Catalonia, Barcelona, in 1997, 2000 and 2003, respectively. Since 2011, he has been a Full Professor with the Department of Energy Technology, Aalborg University, Denmark. From 2015 he is a distinguished guest Professor in Hunan University. His research interests mainly include power electronics, distributed energy-storage, and microgrids. Prof. Guerrero is an Associate Editor for the IEEE TRANSACTIONS ON POWER ELECTRONICS, the IEEE TRANSACTIONS ON INDUSTRIAL ELECTRONICS, and the IEEE Industrial Electronics Magazine, and an Editor for the IEEE TRANSACTIONS on SMART GRID and IEEE TRANSACTIONS on ENERGY CONVERSION. In 2014, 2015, and 2016 he was awarded by Thomson Reuters as Highly Cited Researcher, and in 2015 he was elevated as IEEE Fellow for his contributions on distributed power systems and microgrids.